ADVANCED MATERIALS
www.advmat.de

Interplay of Octahedral Tilts and Polar Order in $BiFeO_3$ Films

*Young-Min Kim, Amit Kumar, Alison Hatt, Anna N. Morozovska, Alexander Tselev, Michael D. Biegalski, Ilya Ivanov, Eugene A. Eliseev, Stephen J. Pennycook, James M. Rondinelli, Sergei V. Kalinin, and Albina Y. Borisevich**

Engineering the electronic structure at transition metal oxide (TMO) interfaces through controlled layer-by-layer thin film growth techniques is a powerful paradigm to stabilize new phases of matter absent in bulk equilibrium phase diagrams.[1] The emergence of such functional states relies on the ability to combine structurally similar TMOs with vastly different electronic properties through choices in chemistry,[2] lattice stresses,[3] orbital interactions of ferroelectric polarization[4] or orbital discontinuities,[5] or magnetic coupling[6] to enable novel device functionalities[7] including high-density 2DEG,[8,9] and functional piezo-, ferro- and magnetoelectricity in oxide thin films.[4,10–14] Recently, however, the importance of octahedral tilts, which are critical in preserving the corner-connectivity of the transition metal BO_6 octahedra across interfaces, to properties of thin films has become recognized.[15–18] Here, we report heterointerface stabilization of a distinct nonpolar $BiFeO_3$ phase occurring simultaneously with changes in octahedral tilts. The resulting phase arises via suppression of polarization by a structural order parameter and can thus be identified as anti-ferroelectric; small antipolar cation displacements can also be detected. This phase is metastable and can be switched into a polar ferroelectric state under an applied electric bias. This finding paves the way towards functional heterostructure devices with multiple-level electronic and magnetoelectric states based on atomic level interfacial chemical and structural control.

In perovskite oxides, the magnitude and sense of rotations of adjacent BO_6 units determines their functional electrical and magnetic properties,[19–21] yet direct external control over the octahedral framework to realize new phases is challenging because the rotations do not respond to electric fields. Interfacial strain and chemistry can affect the rotations of the BO_6 units through a ferroelastic interaction,[22–27] which is microscopically similar to the conventional strain–polarization coupling in polar perovskite oxide thin films and superlattices.[28] While the crucial role of octahedral tilts in ferroelectric behavior has long been understood from the studies of bulk materials (see for example work by Levin et al. and Woodward et al.[29,30]), their influence on the properties of thin films has only recently been documented.[15,26] These behaviors are particularly important in the context of polar oxides, where external electric fields are able to switch the polarization direction, resulting in a field-tunable ground state. To achieve the same dynamic control of the octahedral framework in a perovskite thin film would require either reversing the strain state completely – a practically and technologically ineffective approach – or developing alternative routes.

$BiFeO_3$ (BFO) is the quintessential room temperature multiferroic which normally exhibits a large ferroelectric polarization of ≈90 μC/cm^2.[31] It possesses an intricate set of structural transitions as a function of temperature, pressure, epitaxial strain, or chemical pressure.[31,32] A metastable antiferroelectric (AFE) phase can be induced through isovalent substitution of Bi by smaller rare-earth cations which occurs simultaneously with an anti-ferrodistortive change in the octahedral rotations from $a^-a^-a^-$ to $a^-a^-c^+$.[33] Here we demonstrate that a nonpolar phase can be stabilized through heteroepitaxy that occurs with simultaneous changes to the octahedral tilts at the interface. In addition, through mesoscopic piezoresponse force microscopy, we demonstrate electric field switching between the substrate termination-induced nonpolar and the normal fully polar state. We also observe small antipolar cation displacements in nonpolar phase, thus strongly suggesting that this phase has

Dr. Y.-M. Kim, Dr. S. J. Pennycook, Dr. A. Y. Borisevich
Materials Science and Technology Division
Oak Ridge National Laboratory
Oak Ridge, Tennessee 37831, USA
E-mail: albinab@ornl.gov
Dr. Y.-M. Kim
Division of Electron Microscopic Research
Korea Basic Science Institute
Daejeon 305-806, Korea
Dr. A. Kumar, Dr. A. Tselev, Dr. M. D. Biegalski, Dr. I. Ivanov, Dr. S. V. Kalinin
The Center for Nanophase Materials Sciences
Oak Ridge National Laboratory
Oak Ridge, Tennessee 37831, USA
Dr. A. Hatt
Molecular Foundry
Lawrence Berkeley National Laboratory
Berkeley, California 94720, USA
Dr. A. N. Morozovska
Institute of Physics
National Academy of Sciences of Ukraine
46, pr. Nauki, 03028 Kiev, Ukraine
Dr. E. A. Eliseev
Institute for Problems of Materials Science
National Academy of Science of Ukraine
3, Krjijanovskogo, 03142 Kiev, Ukraine
Prof. J. M. Rondinelli
Department of Materials Science and Engineering
Drexel University
Philadelphia, PA 19104, USA

DOI: 10.1002/adma.201204584

© 2013 WILEY-VCH Verlag GmbH & Co. KGaA, Weinheim

anti-ferroelectric nature. Using real-space electron microscopy imaging techniques combined with first-principles density functional calculations, we describe how the energetic stability of the polar and antipolar displacements is influenced by the octahedral structure, which at the interface should be sensitive to the chemistry of the terminating layer.

The stability of the polar BFO phase is determined by the misfit strain, the interface charge, and the octahedral tilt patterns at the heterointerface. Of these, the tilt pattern is specific to each substrate and cannot be altered post-growth. While it is possible to choose substrates with different tilt patterns, this often requires a change in chemistry of the substrate, leading to different lattice constants and misfit strains, which preclude direct probing of the intrinsic effect of octahedral rotations on the phase stability of the film. In this work, we adopt an alternative strategy: we tune only the layer sequence of the substrate, without changing the overall chemical composition by switching the interface termination during growth. This preserves the strain state and should maintain the octahedral tilt structure of the substrate. The formal charge discontinuity, which is reversed in this case, could affect the stability of the ferroelectric domain orientations in the film, but is expected to interact only weakly with the rotation patterns. At the same time, the structural aspect of the altered layer sequence (AO or BO_2 termination) could affect phase stability in the film near the interface through changes in octahedral tilts at the interface (since rotations are largely stabilized by *A*-site–oxygen interactions in perovskites), bringing the polar and nonpolar phases close in energy to allow for reversible and potentially hysteretic switching.

Previous work by Yu et al.[34] showed that changing interface termination can switch bulk polarization of BFO. In this study, we aim to explore the stability of the polar phase in the near-interface region with changes in termination layer. To explore this, a series (10, 20, 50, 100 nm in thickness) of BFO films was grown on STO substrates with 5 nm LSMO buffer layers using pulsed laser deposition. As $SrTiO_3$ is predominantly TiO_2 terminated, routine STO-LSMO-BFO growth without selective etching gives rise to a (MnO_2)-(BiO) layer sequence at the interface (structure A). To access the (La,SrO)–(FeO_2) interface (structure B), we reverse the LSMO termination by depositing an extra SrO layer on the STO substrate. **Figure 1**a,b show annular dark field (ADF) scanning transmission electron microscopy (STEM) images for 50 nm thick [110] pseudo-cubic ($[110]_{pc}$) oriented BFO thin films grown on the different terminations of LSMO. In this imaging mode, the column intensity is roughly proportional to the square of atomic number.[35] Therefore, we can track interface termination via ADF intensity traces (green graphs in the insets on Figure 1a,b); different ordering of atomic columns in the two panels is evident. The different interface structures of BFO-LSMO were also directly verified by electron energy loss spectroscopy (EELS) line scans; the compositional profiles and the corresponding ADF intensity traces are given in Figures 1c,d. In structure A the integrated signal of the Mn L-edge (red curve) propagates further across the interface compared to the La M signal (green curve, see Figure 1c), demonstrating that the surface of LSMO is indeed terminated by a MnO_2 layer. For structure B, the order of the Mn L and La M curves is reversed, confirming the (La,Sr) O termination (Figure 1d).

We further use the ADF and bright field (BF) STEM images to measure the atom positions at the heterointerface. This way, the polarization behavior, change in lattice spacing (ADF)[15,36–39] and the octahedral rotation angles (BF)[15,36] can be tracked for each unit cell; the schematic in Figure 1e illustrates the quantification procedure for the $[110]_{pc}$ oriented BFO film. Note that the optimal conditions for mapping octahedral tilts using BF STEM will depend on the sample thickness and can differ from the optimal ADF STEM conditions. Here, we have used image simulations to establish the optimal BF conditions for oxygen detection to enable accurate measurements of octahedral tilts (Figure S1 in the Supporting Information). **Figure 2**a,b show BF STEM images for structures A and B. In these optimal conditions, the oxygen columns are the brightest feature in the images. The insets are the corresponding octahedral tilt maps of the images. In these maps, each pixel represents one unit cell; checkerboard contrast reflects antiphase character of the in-plane tilts in both BFO and LSMO, similar to the data reported by Borisevich et al.[15]

Averaging the even (black) and odd (white) "sublattices" of the checkerboard maps along the interface, we obtain the profiles in Figure 2c,d. Clear differences in the tilt behavior at the interface are observed for the two LSMO terminations. For structure A, full suppression of the octahedral rotation angles is observed at the BFO-LSMO interface ($\theta \approx 0°$) that persists for ≈3 atomic layers into BFO; after that the rotation angles gradually increase until around ≈3 nm into BFO when the rotations recover to the bulk BFO values (≈10.5° for this projection, see Figure 2c). In the lateral dimension along the interface, the octahedral rotation suppression is found to persist for multiple tens of nanometers, albeit coexisting with small (<5 nm) regions with incomplete tilt suppression (similar to structure B described below). Similar interface features were observed in heteroepitaxial films grown in two independent batches. Incomplete tilt suppression, however, is observed at the interface for structure B with the angles decreasing to about $\theta \approx 4°$ in comparison with $\theta \approx 7°$ in LSMO. Intriguingly, further into the BFO film of structure B the rotation angles do not recover to the bulk value within the field of view of the image (≈4 nm of BFO) and instead stay at $\theta \approx 4$–$6°$. The interface-induced rotation angle modification in structure B is relatively long range, extending well beyond the thin interface layer, suggesting the stabilization of a distinct interface phase. For both films, however, we find the FeO_6 rotation angles do eventually reach the bulk value at ≈20 nm away from the interface (Figure S2 in the Supporting Information). These results indicate a clear dependence of the near-interface BFO phase stability on the interface termination.

We further characterize the polarization behavior of the two films by mapping the relative cation displacements as a function of the distance from the interface. Figure 2e,f show out-of-plane (*dz*, normal to the interface) displacement maps overlapped with the corresponding ADF STEM images, and the profiles computed from the maps. For structure A (Figure 2e) we observe nonzero displacements starting at the interface, indicative of a polar domain that saturates within 5-6 unit cells. Interestingly, the mapping across the full field of view reveals two domains of opposite polarization, separated by an irregularly-shaped tail-to-tail domain wall (marked as dotted line, see

© 2013 WILEY-VCH Verlag GmbH & Co. KGaA, Weinheim
Adv. Mater. **2013**,
DOI: 10.1002/adma.201204584

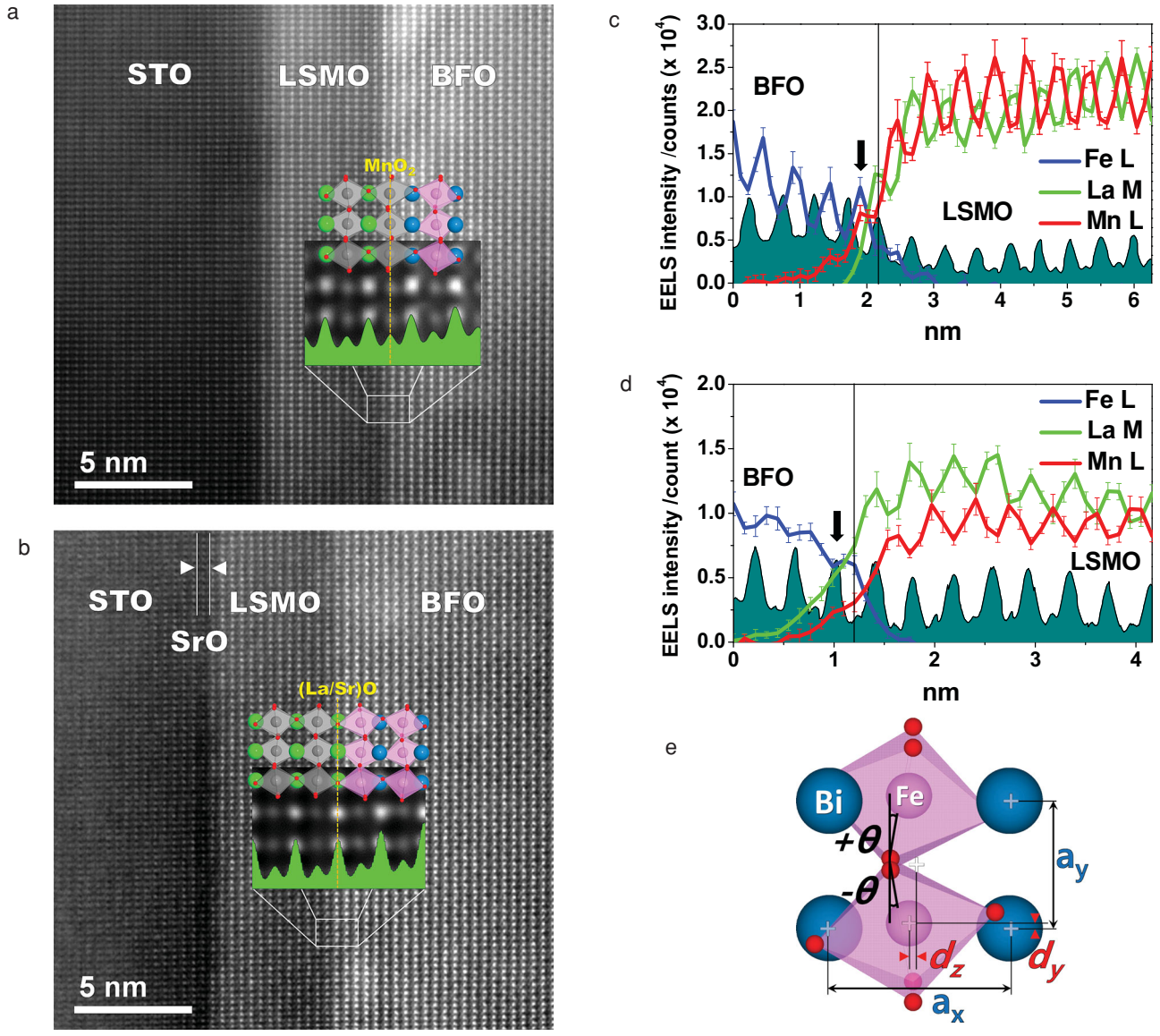

Figure 1. Thin film structures and interface terminations: ADF images of [110] pseudo-cubic oriented BFO thin films grown on: a) MnO_2-terminated LSMO and b) (La,Sr)O-terminated LSMO. The interface termination of LSMO was engineered through surface termination control of the STO substrate by introducing a SrO monolayer (dark layer in (b)). The magnified interfaces in both BFO-LSMO structures with atomic models are displayed as insets in (a) and (b), respectively. c,d) STEM-EELS results obtained across the respective interfaces of BFO-MnO_2-terminated LSMO and BFO-(La,Sr)O-terminated LSMO. e) Schematic to describe the structural parameters of a BFO unit cell oriented to the $[110]_{pc}$ direction that can be measured in STEM image, the lattice spacings (out-of-plane a_x and in-plane a_y), cation displacements (out-of-plane d_z and in-plane d_y) and octahedral tilt ($\pm\theta$).

Figure S3 in the Supporting Information for a larger view). The top domain (with respect to the surface of the film; right on Figure 2) is consistent with the overall film polarization while the opposite orientation is only present in the interface region. This unanticipated feature suggests a complex system of charge compensation at the interface and in the bulk-portion of the film. Note that for the small phase fraction where incomplete octahedral tilt suppression is observed in structure A, an antipolar Bi–Bi modulation also occurs (Figure S4 in the Supporting Information). Nevertheless, the majority volume fraction of all structure A BFO films appear to be ferroelectric, possessing polar cation displacements beginning at the interface.

In marked contrast, structure B (Figure 2f) shows zero net out-of-plane polarization in the near-interface region (i.e., $dz \approx 0$). The nonpolar state persists within the entire field of view of the image (>7 nm of BFO) and correlates with the region of the long-range partial tilt suppression (Figure 2d). Importantly, polarization and tilt values are uniform within these regions and change abruptly to bulk BFO values at well-defined interfaces. This uniformity of crystallographic structure over 5–15 nm scale and abrupt atomically thin boundaries allow us to identify it as an interface-stabilized phase. Clearly, this distinct phase arises via suppression of polarization by a structural order parameter and can thus be considered anti-ferroelectric

© 2013 WILEY-VCH Verlag GmbH & Co. KGaA, Weinheim

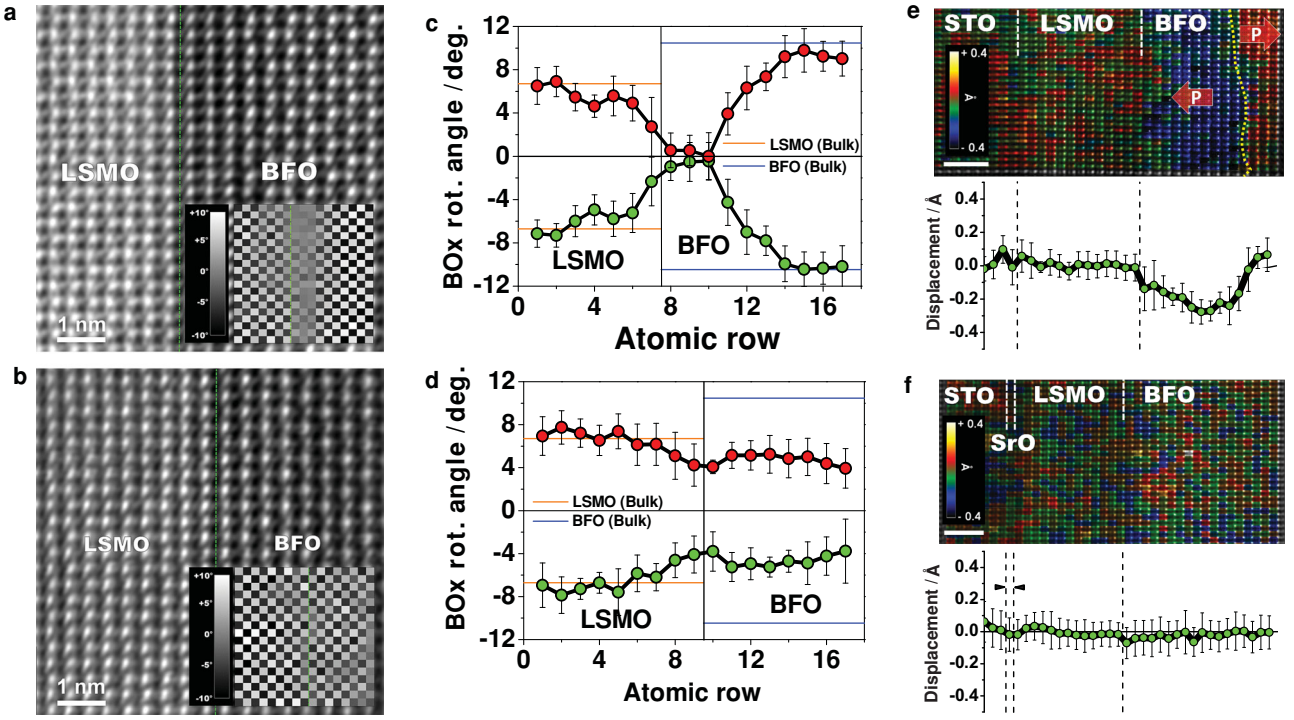

Figure 2. Octahedral tilt and polarization mapping: BF STEM images taken in optimal conditions for oxygen column contrast in the $[110]_{pc}$ oriented BFO film structures grown on: a) MnO_2-terminated LSMO and b) (La,Sr)O-terminated LSMO. The resulting octahedral tilt maps (insets) show checkerboard pattern of tilt angles. c,d) Line profiles of octahedral tilts averaged over vertical rows of the respective tilt maps in (a) and (b). Solid lines in each graph represent tilt angles in the bulk BFO and LSMO. e,f) Out-of-plane (*dz*) displacement maps and the corresponding averaged line profiles of B-site cations in both BFO thin film heterostructures, showing the polarization behavior (data given on the same scale for both films). The maps are overlaid on the respective ADF STEM images. The scale bars are 2 nm.

according to definition by Balashova and Tagantsev[40] (alternative definitions, such as characteristic *P–E* double loop, do not provide any structural criteria and are insufficiently specific (e.g., ferroelectrics above T_c can also show double loops)). Confirming this classification, small (close to detection limit) antipolar in-plane displacements attributed to modulations in the Bi atomic columns were observed in structure B (Figure S5 in the Supporting Information); in the structure A, antipolar displacements were only observed next to the small regions with incomplete suppression of octahedral tilts (Figure S4 in the Supporting Information), suggesting that the nonpolar phase coincides with a metastable AFE phase of BFO with different octahedral rotations. These results suggest that the heterointerface termination mediates the interplay between local cation displacements, electric polarization and octahedral rotation behaviors.

The structural distortions and interface-induced nonpolar phase extend for large distances (3–15 nm) into the film. At these length scales, ferroelectric properties and bias-induced phase transitions between nonpolar and polar states may be indirectly accessed by piezoresponse force microscopy (PFM).[41–43] We note that direct measurements of the antiferroelectric-like hysteresis loop by PFM are complicated even for prototypical AFE materials such as $PbZrO_3$.[44] In many cases, materials showing constricted *P–E* macroscopic hysteresis loops yields FE like hysteresis loops on the nanoscale.[45] From STEM data, the materials studied here are the mixture of nanometer scale mesoscopic FE and AFE regions, and hence measured PFM signal will contain contributions from both states and will be dominated by FE response (since the response of the AFE phase is zero).

To explore the domain structure and polarization switching in these systems systematically, we performed PFM imaging, domain writing, and hysteresis loop measurements. For structure A, the PFM images indicate the presence of classical stripe-like domain structure formed by 50–80 nm size domains for all film thicknesses, **Figure 3**a–c, in agreement with previous studies for similar films.[46,47] For structure B in the 10 nm film (Figure 3d), however, the regular domain structure is absent and the images show considerably reduced average amplitude of the PFM signal. This data is consistent with coexistence of nanoscale polar regions with random polarization orientation and nonpolar regions (despite the high quality of the surface). Large regular domain patterns are observed only for the 20 and 100 nm films (Figure 3e,f). The morphology of these domains is markedly different from the structure A series and is more rounded. X-ray diffraction studies (see Supporting Information) also confirm the absence of domain walls in the 10 nm structure B film.

This field-induced transitions and polarization dynamics in these materials are explored through the polarization switching experiments illustrated in **Figure 4**. While all films exhibit classical switching behavior (similar PFM amplitude in upward-polarized, downward-polarized, and pristine regions, 180 phase change at the domain boundaries), the 10 nm film with structure B shows more complex behavior somewhat

© 2013 WILEY-VCH Verlag GmbH & Co. KGaA, Weinheim
Adv. Mater. **2013**,
DOI: 10.1002/adma.201204584

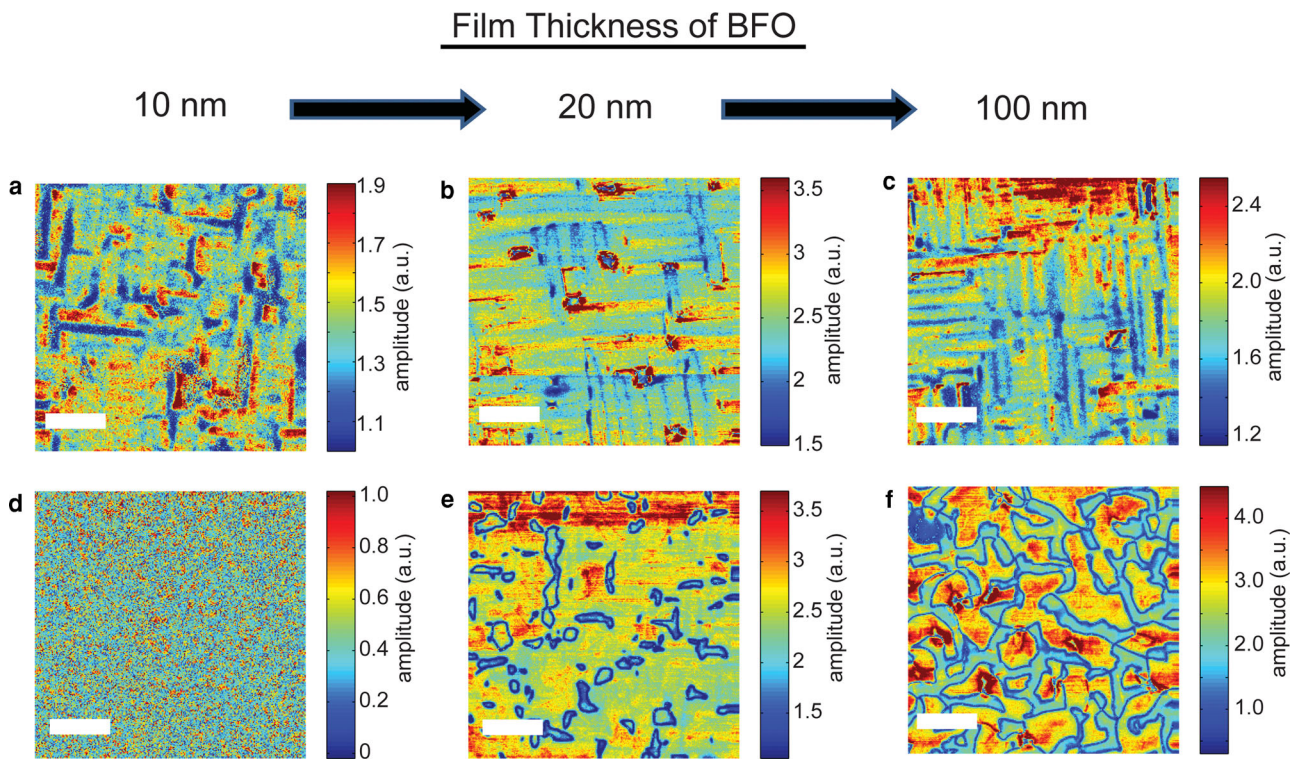

Figure 3. Domain structure evolution and polarization switching: PFM amplitude data series recorded as a function of BFO film thickness grown on (a to c) MnO_2-terminated LSMO and (d to f) (Sr,La)O-terminated LSMO, respectively. The scale bars are 400 nm.

reminiscent of ferroelectric relaxors.[45,48–51] Here, while the pristine regions show contrast consistent with noise or ultra-small polar clusters, poling produces uniformly polarized ferroelectric regions that can be further switched similar to the response of a normal ferroelectric. This behavior is consistent with the coexistence of FE and AFE phases, since the application of sufficiently strong field results in AFE-FE transition and formation of remnant FE-like state that can be visualized by PFM.

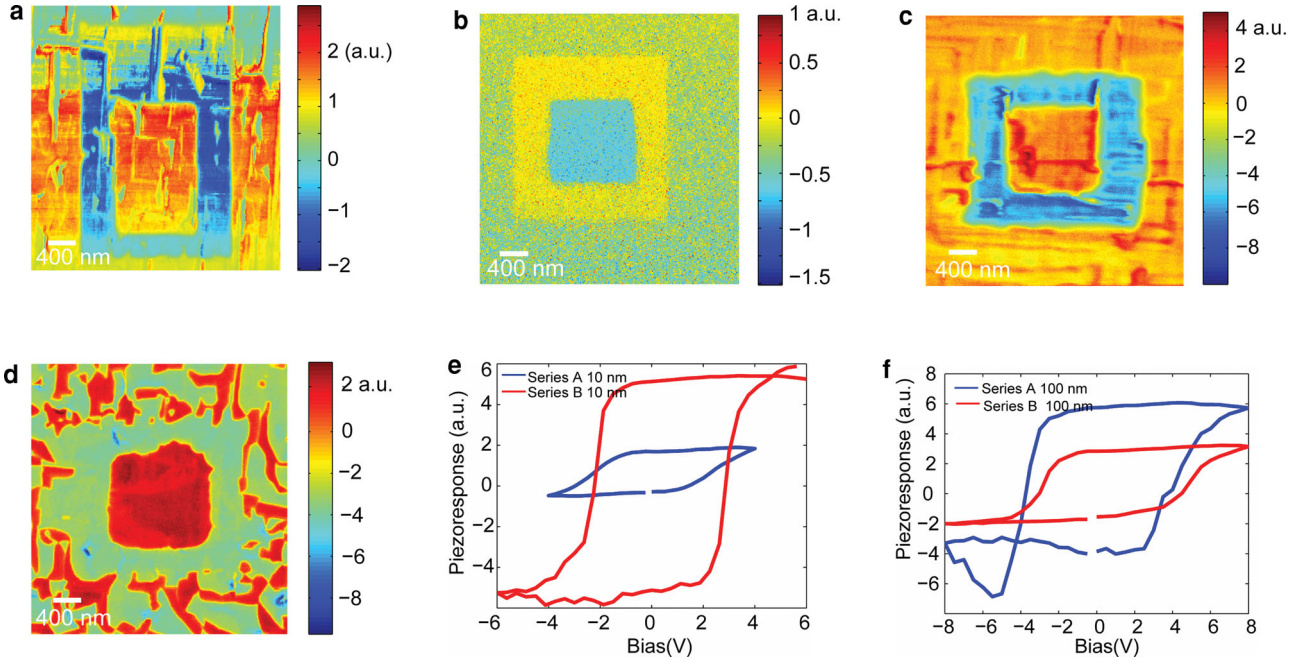

Figure 4. Ferroelectric domain pattern formed by application of +4 V over 2 um and subsequently −4 V over 1 um in: a) 10 nm-thick BFO grown on MnO_2-terminated LSMO, b) 10 nm-thick BFO grown on (La,Sr)O-terminated LSMO, c) 100 nm-thick BFO grown on MnO_2-terminated LSMO, and d) 100 nm-thick BFO grown on (Sr,La)O-terminated LSMO. Hysteresis loops for the 10 nm-thick films are shown in (e) and PFM hysteresis loops for 100 nm thick films are shown in (f).

© 2013 WILEY-VCH Verlag GmbH & Co. KGaA, Weinheim

Finally, the PFM hysteresis loop is significantly smaller for structure B for 10 and 20 nm thicknesses, with the maximal difference observed in the 10 nm films. For 100 nm thick films, structure B has a slightly larger loop. These observations are consistent with the presence of the AFE layer (which does not span the thickness of the film) in the structure B series films, the effect of which is most pronounced in the thinnest film. We further note that attempts to explore polarization switching at higher biases are limited by the dielectric strength of the films. Overall, while PFM cannot establish the AFE nature of material unambiguously (since the signal is dominated by the presence of FE component), it illustrates the (a) nanophase structure of pristine region B and (b) field induced transition to long lived FE state.

To gain insight into the role of octahedral rotations on the BFO film and on the presence of the AFE or FE domains, we perform first-principles density functional calculations. We evaluate the interaction between polar and antipolar atomic displacements for three possible BFO structural variants at the bulk level (sans substrate and strain to extract the intrinsic interaction between ferro- and anti-ferrodistortive distortions) distinguished by octahedral rotation that are consistent with our experimental observations. The possible octahedral rotation patterns examined possess either in-phase (+) or out-of-phase (–) rotations of adjacent FeO_6 octahedra about the out-of-plane axis (**Figure 5**a). We consider three patterns of rotations: the BFO bulk $a^-a^-a^-$ rotations (out-of-phase rotations about all axes), $GdFeO_3$-like $a^-a^-c^+$ rotations (out-of-phase rotations about in-plane axes and in-phase rotations about the out-of-plane axis), and a superposition of the two, an $AgNbO_3$-like $a^-a^-c^-/a^-a^-c^+$ pattern,[52] with a sequence of two in-phase and two out-of-phase rotations about the out-of-plane axis, quadrupling the primitive unit cell. Note that for all of these cases considered, the out-of-phase in-plane octahedral rotations that give rise to "checkerboard" tilt angle maps in STEM are preserved in the calculations. For these three rotation patterns, we evaluated a number of possible FE and AFE configurations by fully relaxing the atomic positions in various symmetries, while maintaining the bulk lattice parameters. Table S1 in the Supporting information enumerates the lowest energy crystal symmetries obtained from this analysis. We focus now on the polar and antipolar atomic displacements in these low-energy structures.

To understand how octahedral rotations could stabilize the nonpolar BFO state at the heterointerface, we consider the relative energetics of the polar and antipolar displacements of these low-energy structures. Figure 5b,c shows the change in energy for each rotation pattern as the amplitude of the polar or antipolar atomic displacement patterns are gradually increased. Here, zero-percent amplitude corresponds to a BFO structure with the reference symmetry (Supporting Information, Table S1), obtained by removing all secondary cation and oxygen displacements that are not rigid-unit mode rotations of the FeO_6 octahedra. From this analysis, we find that the FE and AFE structures are all close in energy, and importantly, that the preference of BFO to adopt a FE or AFE state is intimately linked to the geometric rotation pattern of the FeO_6 octahedra: Figure 5b illustrates that the lowest energy FE state prefers all out-of-phase rotations of the octahedral ($a^-a^-a^-$) while an AFE configuration with the same rotation pattern is substantially higher in energy (Figure 5c). The AFE configuration, rather, is energetically stabilized by in-phase rotations – the $a^-a^-c^+$ rotation pattern being the lowest energy configuration. Furthermore, we find that the energy distortion curves for the AFE $a^-a^-c^+$ (*Pnma* symmetry) and complex tilt (*Pbcm* symmetry) resemble a single parabola shifted to have a nonzero minimum with respect to amplitude

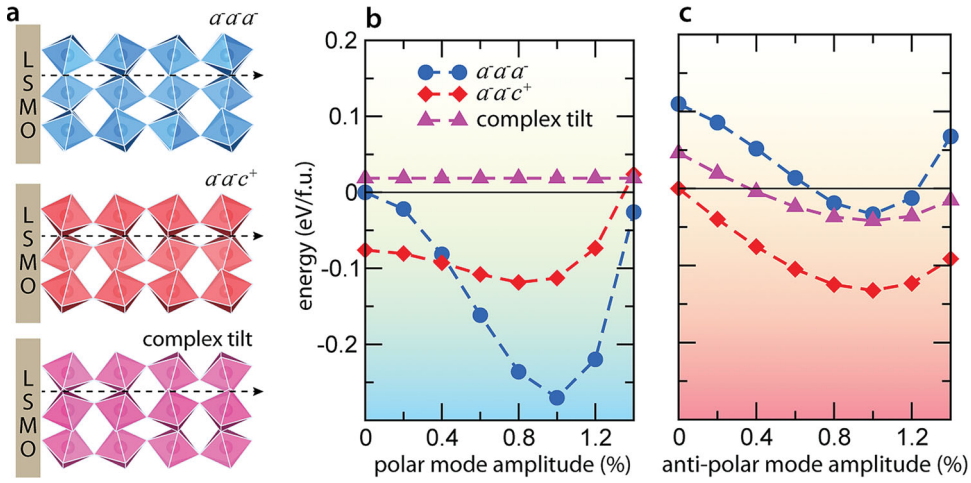

Figure 5. The first-principles calculated FE and AFE energy stabilizations obtained from changes in the BFO octahedral rotation patterns reveal a stronger interaction between the stable electronic state and the geometric connectivity of the octahedral rotations. a) The three structural configurations for BFO (the cations are omitted for clarity) consist of FeO_6 octahedra that rotate (upper) out-of-phase in all directions, $a^-a^-a^-$, (center) out-of-phase in the epitaxial plane and in-phase along the film normal $a^-a^-c^+$, (lower) or in complex tilt pattern given as a superposition of the previous tilt patterns, i.e. $a^-a^-a^-/a^-a^-c^+$. The sense of rotation is distinguishable by the change in shading of the octahedral along the film normal direction indicated by the broken line. b) With increasing amplitude of the polar distortion compatible with the symmetry of the octahedral tilt patterns, the $a^-a^-a^-$ bulk rotation pattern is energetically more favorable than the alternatives. c) In contrast, the antipolar distortions are energetically disfavored in the bulk-like pattern, whereas they are more energetically favorable when in-phase rotations of the FeO_6 octahedra are present in the structure. The energies in panels (b) and (c) are given relative to the lowest polar or antipolar configuration, respectively.

© 2013 WILEY-VCH Verlag GmbH & Co. KGaA, Weinheim
Adv. Mater. **2013**,
DOI: 10.1002/adma.201204584

of the antipolar distortion. This behavior reflects the fact that the antipolar displacements are symmetry allowed in the undistorted phase, i.e. their presence does not require a change in symmetry (Supporting Information, Table S1). As a result, once the octahedral rotation pattern is adopted, the antipolar distortions can be activated through anharmonic interactions without the need for softening a Raman active phonon.

We can now ask what feature of the heterostructures determines the rotation pattern adopted by the BFO film? Based on these results, we argue that the interface selection of the FE or AFE state is due to the preference of the two LSMO interface terminations to stabilize either an in-phase or out-of-phase rotation pattern in the BFO about the film-normal direction. The MnO_2-terminated interface enables the BFO film to have a complete FeO_6 octahedron, and as in the bulk, the film would prefer to adopt the $a^-a^-a^-$ rotation pattern which is energetically more favorable when polar atomic displacements are present. In contrast, the (La,Sr)O/FeO_2 termination leads to FeO_6 octahedra with nearest-neighbor interactions determined by both La/Sr and Bi cations. Because $LaFeO_3$ exhibits, and $SrFeO_3$ has structural tendencies to, the $a^-a^-c^+$ tilt pattern, the asymmetric *A*-site environment surrounding the interfacial FeO_6 octahedra would prefer that the BFO rotation pattern locally adopts in-phase rotations about the film normal as a means to lower the overall energy, while retaining finite out-of-phase rotations in-plane. The in-phase rotations of the low-energy $a^-a^-c^+$ rotation pattern about the film normal direction are consistent with the experimental observed net overall reduction of the in-plane out-of-phase rotations across the interface, rather than a complete suppression. The AFE state emerges since the octahedral rotation patterns are particularly sensitive to the *A*-site environment, which appears in our bulk calculations as splitting in the Bi-Bi pair-distribution function relative to the bulk FE *R*3*c* structure (Figure S6,S7 in the Supporting Information), consistent with the experimental values (± 0.06–0.08 Å).

We note that while the change in predominant polar order for the films with different surface terminations is quite clear, the small proportion of the AFE phase found in the mostly ferroelectric structure A underscores the small energy difference between the two phases for these two heterostructures. Thus, we can expect the AFE state to be strongly affected by local disorder, with each defect a potential nucleation center for the FE phase, and vice versa. From that point of view, the appearance of the nonpolar phase, in addition to a given layer order, can also hinge on the presence or absence of a specific type of defect at a specific concentration, conceivably altering the stability window of the AFE phase for different growth methods or characteristic defect chemistries. Nonetheless, for the case of the films used in this study there is no reason to suspect a difference in global defect compositions between the films with different terminations. Therefore modifying the intimate structural interplay between rotation patterns and polar and antipolar displacements through heteroepitaxial constraints offers a promising route to control polar order in perovskite oxides. Analysis using Landau–Ginsburg–Devonshire theory allows further generalization of this behavior by considering the contributions from changes in interfacial dipoles, surface energy, and the sign of biquadratic tilt-polarization coupling (see Equation S1–S3 and Figure S8 in the Supporting Information).

To summarize, we observe an AFE $BiFeO_3$ phase stabilized via control of the substrate termination concomitant with a change in octahedral tilts across the interface. The interplay of polarization and octahedral tilt behavior underpinning this phase formation is visualized directly on a single unit-cell level though direct order parameter imaging by ADF and BF STEM that allows precise localization of light (oxygen) and heavy (cations) columns and is captured in our bulk level density functional calculations. The nonpolar phase is stabilized over mesoscopic distances, and sharp boundaries between nonpolar and ferroelectric phases of BFO are observed. Relaxation of interface constraints within the film or application of external electric field transforms the material to the ferroelectric state. Exploiting heteroepitaxial routes to control the interplay between octahedral rotations and polar or antipolar displacements will be important for future device applications based on multi-state configurations and readily motivate further investigations into the complex structural coupling available at perovskite oxide interfaces.

Supporting Information

Supporting Information is available from the Wiley Online Library or from the author.

Acknowledgements

This research was supported in part by the U.S. Department of Energy (DOE), Basic Energy Sciences (BES), Materials Sciences and Engineering Division (A.Y.B., Y.M.K., S.V.K., A.K.), and through a user project supported by ORNL's Shared Research Equipment (ShaRE) User Program (YMK, AYB), which is also sponsored by DOE-BES. Computational work (A.H.) was performed at the Molecular Foundry and supported by the Office of Science, Office of Basic Energy Sciences, of the U.S. Department of Energy under contract no. DEAC02-05CH11231. Calculations were performed on the Lawrencium computer cluster at Lawrence Berkeley National Laboratory. J.M.R. was supported by the U.S. Office of Naval Research, under grant number N00014-11-1-0664. The samples used in this study were provided by Ying-Hao Chu and Pu Yu (UC Berkeley). The authors thank Ian Reaney for fruitful advice, and express deep gratitude to Ramamoorthy Ramesh for consistent encouragement and advice throughout this work.

Received: November 5, 2012
Revised: January 4, 2013
Published online:

[1] H. Y. Hwang, Y. Iwasa, M. Kawasaki, B. Keimer, N. Nagaosa, Y. Tokura, *Nat. Mater.* **2012**, *11*, 103.
[2] P. Zubko, S. Gariglio, M. Gabay, P. Ghosez, J. M. Triscone, *Annu. Rev. Condens. Matter Phys.* **2011**, *2*, 141.
[3] A. Ohtomo, D. A. Muller, J. L. Grazul, H. Y. Hwang, *Nature* **2002**, *419*, 378.
[4] S. Mathews, R. Ramesh, T. Venkatesan, J. Benedetto, *Science* **1997**, *276*, 238.
[5] A. V. Boris, Y. Matiks, E. Benckiser, A. Frano, P. Popovich, V. Hinkov, P. Wochner, M. Castro-Colin, E. Detemple, V. K. Malik, C. Bernhard, T. Prokscha, A. Suter, Z. Salman, E. Morenzoni, G. Cristiani, H. U. Habermeier, B. Keimer, *Science* **2011**, *332*, 937.
[6] M. Bibes, J. E. Villegas, A. Barthelemy, *Adv. Phys.* **2011**, *60*, 5.

© 2013 WILEY-VCH Verlag GmbH & Co. KGaA, Weinheim

[7] J. Mannhart, D. G. Schlom, *Science* **2010**, *327*, 1607.
[8] Y. Hikita, M. Nishikawa, T. Yajima, H. Y. Hwang, *Phys. Rev. B* **2009**, *79*, 073101.
[9] T. Yajima, Y. Hikita, H. Y. Hwang, *Nat. Mater.* **2011**, *10*, 198.
[10] J. D. Burton, E. Y. Tsymbal, *Phys. Rev. Lett.* **2011**, *106*, 157203.
[11] J. H. Lee, L. Fang, E. Vlahos, X. L. Ke, Y. W. Jung, L. F. Kourkoutis, J. W. Kim, P. J. Ryan, T. Heeg, M. Roeckerath, V. Goian, M. Bernhagen, R. Uecker, P. C. Hammel, K. M. Rabe, S. Kamba, J. Schubert, J. W. Freeland, D. A. Muller, C. J. Fennie, P. Schiffer, V. Gopalan, E. Johnston-Halperin, D. G. Schlom, *Nature* **2010**, *466*, 954.
[12] H. J. A. Molegraaf, J. Hoffman, C. A. F. Vaz, S. Gariglio, D. van der Marel, C. H. Ahn, J. M. Triscone, *Adv. Mater.* **2009**, *21*, 3470.
[13] J. F. Scott, *Science* **2007**, *315*, 954.
[14] R. J. Zeches, M. D. Rossell, J. X. Zhang, A. J. Hatt, Q. He, C. H. Yang, A. Kumar, C. H. Wang, A. Melville, C. Adamo, G. Sheng, Y. H. Chu, J. F. Ihlefeld, R. Erni, C. Ederer, V. Gopalan, L. Q. Chen, D. G. Schlom, N. A. Spaldin, L. W. Martin, R. Ramesh, *Science* **2009**, *326*, 977.
[15] A. Y. Borisevich, H. J. Chang, M. Huijben, M. P. Oxley, S. Okamoto, M. K. Niranjan, J. D. Burton, E. Y. Tsymbal, Y. H. Chu, P. Yu, R. Ramesh, S. V. Kalinin, S. J. Pennycook, *Phys. Rev. Lett.* **2010**, *105*, 087204.
[16] S. J. May, J. W. Kim, J. M. Rondinelli, E. Karapetrova, N. A. Spaldin, A. Bhattacharya, P. J. Ryan, *Phys. Rev. B* **2010**, *82*, 014110.
[17] J. M. Rondinelli, S. J. May, J. W. Freeland, *MRS Bull.* **2012**, *37*, 261.
[18] J. M. Rondinelli, N. A. Spaldin, *Phys. Rev. B* **2010**, *82*, 113402.
[19] R. F. Berger, C. J. Fennie, J. B. Neaton, *Phys. Rev. Lett.* **2011**, *107*, 146804.
[20] P. Garcia-Fernandez, J. A. Aramburu, M. Moreno, *Phys. Rev. B* **2011**, *83*, 174406.
[21] M. Imada, A. Fujimori, Y. Tokura, *Rev. Mod. Phys.* **1998**, *70*, 1039.
[22] P. Aguado-Puente, P. Garcia-Fernandez, J. Junquera, *Phys. Rev. Lett.* **2011**, *107*, 217601.
[23] V. Gopalan, D. B. Litvin, *Nat. Mater.* **2011**, *10*, 376.
[24] S. A. Hayward, F. D. Morrison, S. A. T. Redfern, E. K. H. Salje, J. F. Scott, K. S. Knight, S. Tarantino, A. M. Glazer, V. Shuvaeva, P. Daniel, M. Zhang, M. A. Carpenter, *Phys. Rev. B* **2005**, *72*, 054110.
[25] J. M. Rondinelli, S. Coh, *Phys. Rev. Lett.* **2011**, *106*, 235502.
[26] J. M. Rondinelli, C. J. Fennie, *Adv. Mater.* **2012**, *24*, 1961.
[27] J. M. Rondinelli, N. A. Spaldin, *Adv. Mater.* **2011**, *23*, 3363.
[28] R. E. Cohen, *Nature* **1992**, *358*, 136.
[29] I. Levin, M. C. Stennett, G. C. Miles, D. I. Woodward, A. R. West, I. M. Reaney, *Appl. Phys. Lett.* **2006**, *89*.
[30] D. I. Woodward, I. M. Reaney, R. E. Eitel, C. A. Randall, *J. Appl. Phys.* **2003**, *94*, 3313.
[31] G. Catalan, J. F. Scott, *Adv. Mater.* **2009**, *21*, 2463.
[32] J. X. Zhang, B. Xiang, Q. He, J. Seidel, R. J. Zeches, P. Yu, S. Y. Yang, C. H. Wang, Y. H. Chu, L. W. Martin, A. M. Minor, R. Ramesh, *Nat. Nanotechnol.* **2011**, *6*, 97.
[33] D. Kan, L. Palova, V. Anbusathaiah, C. J. Cheng, S. Fujino, V. Nagarajan, K. M. Rabe, I. Takeuchi, *Adv. Funct. Mater.* **2010**, *20*, 1108.
[34] P. Yu, W. Luo, D. Yi, J. X. Zhang, M. D. Rossell, C. H. Yang, L. You, G. Singh-Bhalla, S. Y. Yang, Q. He, Q. M. Ramasse, R. Erni, L. W. Martin, Y. H. Chu, S. T. Pantelides, S. J. Pennycook, R. Ramesh, *Proc. Natl. Acad. Sci. USA* **2012**, *109*, 9710.
[35] *Scanning Transmission Electron Microscopy*, (Eds: S. J. Pennycook, P. D. Nellist), Springer, New York **2011**.
[36] A. Borisevich, O. S. Ovchinnikov, H. J. Chang, M. P. Oxley, P. Yu, J. Seidel, E. A. Eliseev, A. N. Morozovska, R. Ramesh, S. J. Pennycook, S. V. Kalinin, *ACS Nano* **2010**, *4*, 6071.
[37] H. J. Chang, S. V. Kalinin, A. N. Morozovska, M. Huijben, Y. H. Chu, P. Yu, R. Ramesh, E. A. Eliseev, G. S. Svechnikov, S. J. Pennycook, A. Y. Borisevich, *Adv. Mater.* **2011**, *23*, 2474.
[38] C. T. Nelson, B. Winchester, Y. Zhang, S. J. Kim, A. Melville, C. Adamo, C. M. Folkman, S. H. Baek, C. B. Eom, D. G. Schlom, L. Q. Chen, X. Q. Pan, *Nano Lett.* **2011**, *11*, 828.
[39] Y.-M. Kim, J. He, M. D. Biegalski, H. Ambaye, V. Lauter, H. M. Christen, S. T. Pantelides, S. J. Pennycook, S. V. Kalinin, A. Y. Borisevich, *Nat. Mater.* **2012**, *11*, 888.
[40] E. V. Balashova, A. K. Tagantsev, *Phys. Rev. B* **1993**, *48*, 9979.
[41] N. Balke, I. Bdikin, S. V. Kalinin, A. L. Kholkin, *J. Am. Ceram. Soc.* **2009**, *92*, 1629.
[42] A. Gruverman, A. Kholkin, *Rep. Prog. Phys.* **2006**, *69*, 2443.
[43] S. V. Kalinin, A. N. Morozovska, L. Q. Chen, B. J. Rodriguez, *Rep. Prog. Phys.* **2010**, *73*, 056502.
[44] L. Pintilie, K. Boldyreva, M. Alexe, D. Hesse, *J. Appl. Phys.* **2008**, *103*, 024101.
[45] A. Kholkin, A. Morozovska, D. Kiselev, I. Bdikin, B. Rodriguez, P. P. Wu, A. Bokov, Z. G. Ye, B. Dkhil, L. Q. Chen, M. Kosec, S. V. Kalinin, *Adv. Funct. Mater.* **2011**, *21*, 1977.
[46] F. Zavaliche, R. R. Das, D. M. Kim, C. B. Eom, S. Y. Yang, P. Shafer, R. Ramesh, *Appl. Phys. Lett.* **2005**, *87*, 182912.
[47] F. Zavaliche, P. Shafer, R. Ramesh, M. P. Cruz, R. R. Das, D. M. Kim, C. B. Eom, *Appl. Phys. Lett.* **2005**, *87*, 252902.
[48] F. M. Bai, J. F. Li, D. Viehland, *Appl. Phys. Lett.* **2004**, *85*, 4457.
[49] S. V. Kalinin, B. J. Rodriguez, J. D. Budai, S. Jesse, A. N. Morozovska, A. A. Bokov, Z. G. Ye, *Phys. Rev. B* **2010**, *81*, 064107.
[50] V. Shvartsman, A. Tyunina, J. Levoska, A. Kholkin, *Ferroelectrics* **2004**, *302*, 569.
[51] V. V. Shvartsman, A. L. Kholkin, M. Tyunina, J. Levoska, *Appl. Phys. Lett.* **2005**, *86*, 222907.
[52] I. Levin, V. Krayzman, J. C. Woicik, J. Karapetrova, T. Proffen, M. G. Tucker, I. M. Reaney, *Phys. Rev. B* **2009**, *79*, 104113.

© 2013 WILEY-VCH Verlag GmbH & Co. KGaA, Weinheim
Adv. Mater. **2013**,
DOI: 10.1002/adma.201204584